research

R.Elvin*, M. W. Wright, B. Lewis, B. L. Keliehor, A. Bregazzi, J. P. McGilligan, A. S. Arnold, P. F. Griffin, and E. Riis

Towards a compact, optically-interrogated, cold-atom microwave clock

Abstract: A compact platform for cold atoms opens a range of exciting possibilities for portable, robust, and accessible quantum sensors. In this work we report on the development of a cold-atom microwave clock in a small package. Our work utilises the grating magneto-optical trap and high-contrast coherent population trapping in the lin⊥lin polarisation scheme. We optically probe the atomic ground-state splitting of cold ^{87}Rb atoms using a Ramsey-like sequence whilst the atoms are in free-fall. We have measured a short-term fractional frequency stability of $5\times10^{-11}/\sqrt{\tau}$ with a projected quantum projection noise limit at the $10^{-13}/\sqrt{\tau}$ level.

1 Introduction

In recent years the miniaturisation of quantum sensors, such as atomic clocks, has become increasingly important as the field of applied quantum technologies continues to grow. Devices with laser-cooled atoms at their core benefit from inherently long coherence times provided by the cold atoms in an interaction-free environment. Most notably, highly sensitive cold-atom optical clocks have seen dramatic progress [1, 2, 3, 4], with promising steps towards m^3–scale portable systems [5, 6]. In addition, microwave atomic clocks based on cold atoms with instabilities on the order of $10^{-13}/\sqrt{\tau}$ have become commercially available [7, 8, 9, 10, 11].

With marketable and accessible devices in mind, reducing the footprint is an important step for expanding the versatility of these systems, with the largest hurdle being the necessary bulk of apparatus required for laser cooling. Precise quantum sensors with the ability to be operated outside the laboratory environment would prove to be a valuable goal. A system taking a defining step towards portability is the grating magneto-optical trap (GMOT)[12]. The GMOT is a proven technology, capable of reaching trapped atom numbers on the order of $N \sim 10^8$ from one input beam incident on a microfabricated, diffractive optic. In previous work,

R.Elvin*, M. W. Wright, B. Lewis, B. L. Keliehor, A. Bregazzi, J. P. McGilligan, A. S. Arnold, P. F. Griffin, E. Riis, SUPA, University of Strathclyde, Glasgow G4 0NG, UK. *email: rachel.elvin@strath.ac.uk

the GMOT has demonstrated the ability of reaching molasses temperatures of $T \sim 3\,\mu\text{K}$ with $N \sim 3 \times 10^6$ Rb atoms [13]. We have since improved the atom number to samples of $N \sim 3 \times 10^7$ while still maintaining single-digit μK temperatures. Comparable with regular 6-beam MOTs, the GMOT makes an ideal candidate for compact source of cold atoms in portable atomic clocks, and as a platform for other quantum technologies, such as atom interferometers [14] and quantum memories [15]. GMOT gratings have recently become commercially available [16].

In this paper, we review our cold atom microwave clock based on an ^{87}Rb GMOT apparatus [17, 18]. We investigate the combination of coherent population trapping (CPT) in a pulsed Ramsey-like scheme as an optical probe of the ground-state hyperfine splitting frequency with a sample of cold atoms supplied by the GMOT. The probe consists of a bichromatic field, with components separated by the splitting or clock frequency, that drives atoms into a non-interacting, coherent superposition of the hyperfine ground states. A narrow resonance feature detected in the laser transmission can then be used as a frequency reference, creating the basis for a CPT atomic clock [19].

The CPT technique was important in the realisation of the chip-scale atomic clock (CSAC) [20], and has since been developed into several 'high-contrast' methods that boost the performance of CPT frequency references. The techniques were adapted to capitalise on the constructive interference of dark-state resonances [21] and have been applied in both thermal- and cold-atom CPT clocks. They include techniques such as such as lin||lin [22, 23], lin⊥lin [24, 25, 17], push-pull optical pumping (PPOP) [26] and $\sigma^+ - \sigma^-$ [27, 28, 29]. In the latter three techniques the atoms see the same excitaion field but the way the field is generated is different. In our ^{87}Rb GMOT-CPT apparatus we apply CPT in the lin⊥lin polarisation scheme to achieve a short-term stability of $5 \times 10^{-11}/\sqrt{\tau}$.

2 GMOT Apparatus

In this section, we describe the GMOT experimental apparatus used for laser cooling. Full details have been included in previous papers from the group, for example [13], and we here only provide an overview of the system.

We initially prepare 10^7 atoms in the GMOT using trap and repump light from two external cavity diode lasers (ECDLs), stabilised with saturated absorption spectroscopy. Acousto-optic modulators (AOMs) are used for frequency control and fast power switching, and a mechanical shutter is used for complete extinction of the cooling light during the experiment sequence. Both trap and repump fields are coupled into a common polarisation-maintaining optical fibre that transports the light to a vacuum chamber and grating-chip ensemble, shown in Fig. 1. The chip area

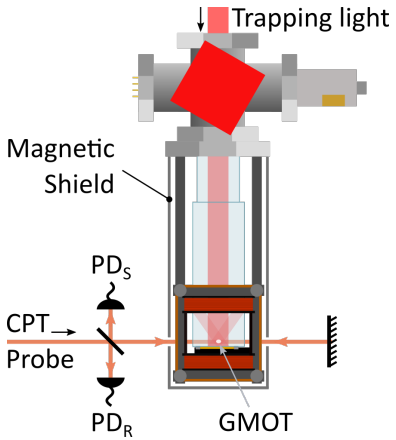

Fig. 1: A top-down view of the clock apparatus that includes the vacuum chamber, ion pump (red square) and magnetic coils. The atoms within a Rb grating magneto-optical trap (GMOT) are probed using coherent population trapping (CPT) in a lin⊥lin polarisation scheme. The clock signal is detected using two photodiodes, PD_S and PD_R, corresponding to detection of CPT signal and a reference photodiode with no atomic signal.

is 20×20 mm^2, with a symmetrical arrangement of three linear gratings etched into its surface [12]. The microfabricated grating is held securely outside of the vacuum chamber, mounted parallel to, and 0.2 mm away from, the glass cell end facet. Other than small intensity losses through the glass walls, mounting the grating chip outside of the vacuum chamber has no observable effect on trapped atom number or temperature.

The trap and repump beams are expanded, collimated, and circularly polarised before being directed through the chamber and onto the grating chip, creating the atom trapping volume from the overlap of incident and diffracted beams. The quadrupole magnetic field for trapping is generated from an anti-Helmholtz coil pair that positions the centre of the trapping region approximately 5 mm above the centre of the grating (~ 3 mm from the cell surface). Three orthogonal pairs of Helmholtz coils are arranged around the chamber in order to cancel the ambient magnetic field at the position of the atoms. One set of the Helmholtz coils, in the direction of the CPT probe, can be used to apply a homogeneous field along this axis to lift the degeneracy on the magnetic sub-levels.

The vacuum chamber, with its attached coil and grating mount, is then enclosed in a cylindrical μ-metal shield with a shielding factor of approximately 100 to reduce sensitivity to ambient magnetic field fluctuations. The complete vacuum system has a volume of approximately 25 litres, with a longest dimension of 60 cm, including the ion pump. The vacuum pressure is maintained by a relatively small ion pump (2 ℓ/s) at around 10^{-7} mbar with electrical feedthroughs connecting to dispensers that provide a controllable source of thermal Rb atoms. The rubidium-dominated pressure provides an intentionally-large atomic density for fast cycle operation while still facilitating atom recapture between experiment cycles, as was previously demonstrated [30]. In this work atomic recapture is not applied for reasons that are explained later in the text.

3 lin⊥lin CPT

Here we detail the CPT technique that is used to optically probe the ground-state hyperfine splitting frequency in alkali atoms [19]. The atoms are pumped into a coherent dark state using a probe beam comprised of two components with a difference in frequency equal to the hyperfine splitting. In this method, the clock signal can be obtained from the transmission of the CPT field probe through the atoms. The detected signal, and therefore the performance of the clock, is then directly related to the dark state population. The technique relies on good phase coherence between the two optical fields in order to maximise the number of atoms that are optically pumped into the dark state [23, 31].

An ideal dark state can be formed between the $|F = 1, m_F = 0\rangle$ and $|F = 2, m_F = 0\rangle$ Zeeman sub-levels using laser light tuned to the D_1 line of ^{87}Rb. This can be accessed using circularly polarised light under a weak magnetic field parallel with the direction of the beam. However, this arrangement leads to poor signal contrast as population collects in the stretched Zeeman sub-levels; for example $|1, 1\rangle$ and $|2, 2\rangle$. To concentrate population in the $m_F = 0$ dark-state, and consequently improve the contrast of the detected CPT signal, arranging for constructive interference of multiple dark resonances is an necessary approach [21, 32]. There are several 'high-contrast' schemes that achieve this using polarisation. Our approach is to adopt the lin⊥lin scheme, where the two CPT field components are orthogonally linearly polarised relative to one another.

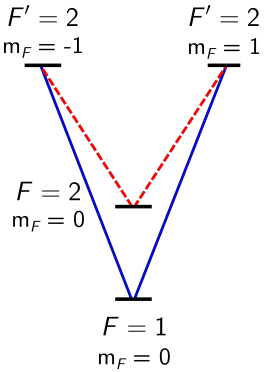

Fig. 2: Level diagram for lin⊥lin CPT on the D_1 line of ^{87}Rb. The dashed-red and solid-blue lines represent the orthogonally polarised CPT fields. The coherent dark state generated with this scheme is between states $|F = 1, m_F = 0\rangle$ and $|F = 2, m_F = 0\rangle$.

As shown by the simplified double-V structure in Fig. 2, the $|F = 1\ \&\ 2, m_F = 0\rangle$ levels are coupled via interaction with the excited $F' = 2$ state. In lin⊥lin CPT, a dark resonance forms between the $m_F = 0$ sub-levels of the $F = 1, 2$ manifolds that can be addressed by both circularly polarised components of the CPT field. The phases of the polarisation components in the lin⊥lin CPT allow for a common dark state to be formed, despite the negative Clebsch-Gordan coefficient associated with one of the D_1 transitions [24, 25]. The two components of the probe beam (shown in red and blue in Fig. 2) form individual

V-systems that contribute equally to the total dark state population [33].

4 Probing the atoms

In our experiment, the clock signal appears as Ramsey-like fringes in the absorption of the probe laser by the cold-atom cloud. The signal is directly related to the population of atoms that are trapped in the dark state. As mentioned in the previous section, an essential component for achieving high CPT contrast is maximising the population of the dark state and reducing the number of atoms occupying the stretched states. In addition, the phase coherence between the CPT fields also plays a role in forming complete dark states [31]. In this experiment, the driving fields that are used to perform lin⊥lin CPT originate from the same laser, giving us inherent phase coherence [17, 18, 33].

The Ramsey-CPT interrogation differs from the traditional Ramsey method in several ways. Instead of two separated $\pi/2$ pulses, with optical pumping for preparation and state detection on either side, Ramsey-CPT is achieved entirely with two pulses from the pump/probe beam. The first interaction is a pulse of the CPT light of sufficient duration and intensity to pump atoms into the dark state. This pulse sets the superposition, after which the atoms are left in the dark for a variable time, T, to allow phase between the atoms and the CPT field to build. A final pulse of the CPT field then maps this accumulated phase into a detectable signal, where the phase difference between atoms and the laser is reflected in the detected absorption. If at the start of the second pulse the atomic superposition and the lasers are out of phase then this corresponds to the bright state of the combined system. The atoms will then be pumped into the dark state, which results in the scattering of light and a reduction of the signal on the photodetector. On the other hand, if the bichromatic laser field and atoms are in phase then this corresponds to a dark state; the atoms are then transparent to the laser field and a maximum in the transmitted light will be observed. The full Ramsey-CPT signal as a function of detuning follows the familiar sinusoidal form observed in traditional Ramsey spectroscopy.

The schematic in Fig. 3 shows how the final lin⊥lin CPT probe is generated from a single ECDL operating at $\lambda_{D1} = 795\,\text{nm}$ and locked via saturated absorption spectroscopy to the $F = 2 \rightarrow F' = 2$ transition. The primary beam at the output of the ECDL is split into two paths that eventually become the two CPT field components, $\text{CPT}_{1,2}$, which are orthogonally linearly polarised and resonant with the D_1 line $F = 1, 2 \rightarrow F' = 2$ transitions, respectively. We use the $F' = 2$ upper excited level to suppress excitation of magnetically sensitive $\Delta m_F = 2$ CPT resonances, formed between the $|F = 1, m_F = \pm 1\rangle$ and $|F = 2, m_F = \mp 1\rangle$ states [32, 33, 34].

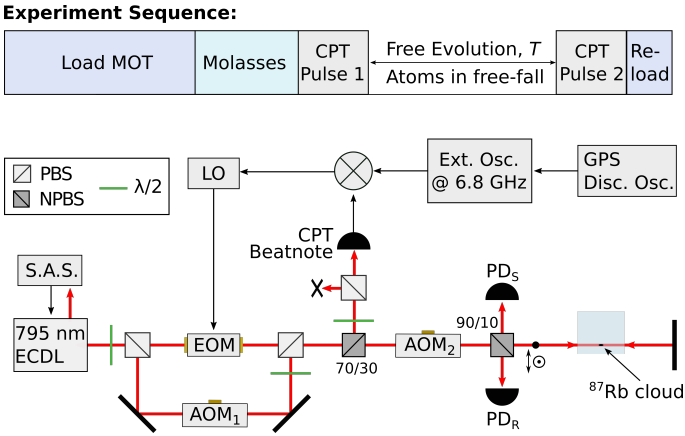

Fig. 3: Top: Experimental sequence that loads atoms into the MOT, cools, and then applies the Ramsey-CPT interrogation. Bottom:Schematic of the CPT optical bench that was used to generate the lin⊥lin CPT fields. PBS and NPBS are polarising and non-polarising beam splitters, respectively. LO is the local oscillator that drives the EOM and sets the two-photon detuning.

In one path, the beam passes through an AOM (AOM_1 in Fig. 3). The beam in the other path is coupled into an electro-optical modulator (EOM) to generate sidebands at $f_{EOM} = f_{HFS} + f_{AOM1}$, where f_{HFS} is the hyperfine splitting frequency of the ground states in ^{87}Rb ($\sim 6.8\,$GHz). The microwave power is set such that each first-order sideband has approximately 30% of the total power. The diffracted beam from AOM_1 and the output light from the EOM are then re-combined on a polarizing beam splitter (PBS) to generate a single beam that is comprised of two orthogonally-polarised fields. In our apparatus, all frequency sources related to the interrogation of the clock transition are referenced to a GPS-disciplined oscillator with a specified stability below the 10^{-12} level.

After re-combination, 70% of the optical power is picked off using a non-polarizing beam splitter (NPBS), with reflected/transmitted ratio = 70/30. The pickoff beam is passed through a half-waveplate and PBS, to overlap the polarizations of all spectral components, and is then measured usimg a fast photodiode to generate a beat-note between the field components that were separated in frequency by f_{HFS}. The beatnote frequency is compared to an additional high-stability frequency source operating around f_{HFS} to generate a error signal that is used in a phase-locked loop (PLL) to suppress extra phase noise at the microwave frequency picked up from the split path [18]. The remaining 30% of the optical power is coupled through a second AOM (AOM_2 in Fig. 3). This shifts the frequencies of the AOM_1 beam

and a single first-order sideband of the EOM light onto resonance with the two CPT transitions that are shown in Fig. 2. Switching of AOM_2 is used for fast extinction of the CPT probe beam during the clock sequence.

A typical Ramsey-CPT sequence is shown in the upper section of Fig. 3. The atoms are loaded into the MOT and then cooled in an optical molasses before the trap and repump light is extinguished using a mechanical shutter. The shutter eliminates light leakage through the AOM used to switch the trap light, which would otherwise result in AC-Stark shifts of the clock frequency. The atoms are then probed whilst in free-fall to obtain our clock signal, with CPT pumping pulses of $\tau_{1,2} = 500\,\mu s$, before the entire sequence repeats.

The CPT probe transmission is detected using two photodiodes, labelled 'PD_S' and 'PD_R', for the 'signal' and 'reference' photodiodes respectively, in Fig. 3. One former photodiode obtains the CPT signal by measuring the probe light after interacting with the cold atoms, while the latter samples the probe light as a reference signal that is then used to cancel common-mode intensity noise on the detected CPT signal. Detecting the transmission of the first pulse lets us obtain the CPT spectrum as the two-photon detuning is scanned by changing f_{EOM}.

We observe Ramsey–CPT fringes by measuring the transmission at the beginning of the second CPT pulse as the two-photon detuning is scanned. The phase information accumulated during the Ramsey sequence can be obtained from the change in transmission within an optical pumping transient at the beginning of the second CPT pulse. The time scale of this transient window is determined purely by the time required to reach steady-state optical pumping. Taking advantage of the optical pumping dynamics, we can apply a second stage of common-mode intensity noise cancellation to the detected fringes by identifying two regions on the detected pulse. The first contains the optical pumping transient and is set to the initial 28 μs, for a total optical power of $P \sim 30$ μW. The length of this region approximately corresponds to the optical pumping time, and therefore depends on the optical power applied [35]. The second region is the last 100 μs of the detected pulse where the transmission has reached a steady-state value. The duration of both regions of interest are found empirically and were individually optimised using the final signal to noise ratio of the fringes as the figure of merit.

The transmission in the first region of the read-out pulse is integrated and normalised against the integrated transmission in the second region to apply the second stage of noise cancellation. This technique reduces the effect of atom number fluctuations, and has been applied before in other similar work, [31]. Additionally, the steady-state transmission of the first detected pulse can be used to suppress against the effect of shot-to-shot atom number fluctuations. An example of Ramsey fringes with a free evolution time of $T = 10\,ms$ is

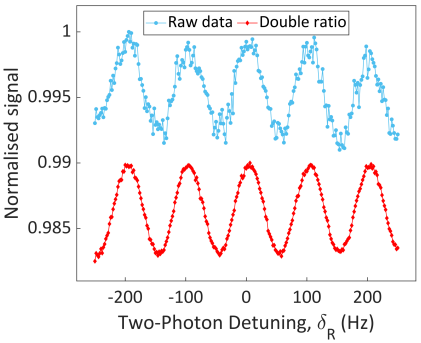

Fig. 4: Scanned Ramsey-CPT fringes with $T = 10$ ms before (blue) and after the noise cancellation is applied (red). Each data point represents a single run of the experiment sequence and the fringes have been offset for clarity.

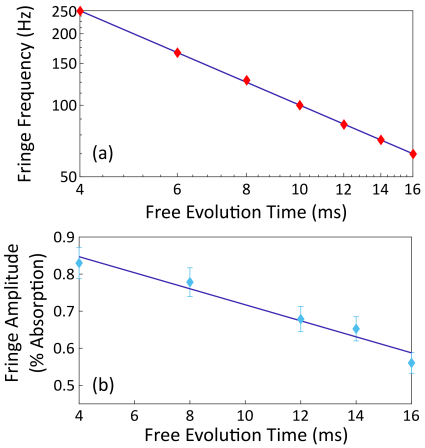

Fig. 5: (a) Frequency of the detected Ramsey fringes as the free evolution time is varied from 4 ms to 16 ms. (b) Amplitude of the fringes, expressed as percentage absorption by normalizing to the probe beam power, as the free evolution time is increased from 4 ms to 16 ms. A straight line has been added to guide the eye. The fringe frequency and peak-peak amplitude in (a) and (b) were obtained using a model fitted to the Ramsey fringes. Note, that the axis axis in (a) is logarithmic and is linear in (b). Errors are one sigma deviations from fits to the raw data across multiple runs. Errors in (a) are included in the data points

shown in Fig. 4 before (blue circles) and after (red diamonds) the double normalisation is applied. The 'raw' data refers to the integrated transmission of the first region on the second pulse without any common-mode noise cancellation applied. The difference in detected signal to noise ratio is approximately a factor of 10, and has a direct effect on the detected short-term frequency stability.

With the Raman-CPT interrogation technique, we expect the fringe frequency to follow a $1/T$ behaviour as the free evolution time is increased. This is observed in the data shown in Fig. 5 (a), as expected, for dark times that range from $T = 4$ ms to $T = 16$ ms. In Fig. 5 (b), the fringe amplitude is observed to decrease linearly with the free-evolution time, T. This behaviour agrees with observations in other work [35], although with a decreased rate of decay, which we attribute to our lower atomic temperature. Since the probe beam diameter is significantly larger than the MOT size, the signal loss is attributed to higher-velocity atoms escaping the interrogation region during the Ramsey time.

5 Clock Stability Performance

In this section, we review the performance of the lin⊥lin CPT experiment with the apparatus described here. We characterize the frequency stability using the central CPT-Ramsey fringe with $T = 10\,\text{ms}$, corresponding to a fringe pattern of 100 Hz. Alternating the frequency of the LO between the two sides of the central fringe allows estimation of the magnitude and direction of shifts of the central fringe. This is a common method of obtaining frequency variations between the atomic resonance and LO. Using the detection method outlined in the previous section, we measure a signal to noise ratio (SNR) on the sides of the Ramsey fringe of ~ 40.

The short-term stability is measured by calculating the overlapping Allan deviation after approximately one hour of measurement time (Fig. 6). These data represent the stability of the free-running central Ramsey fringe. The short-term stability was measured to be $5 \times 10^{-11}/\sqrt{\tau}$, shown by the red dashed line in Fig. 6. The instability measured here is higher than we have presented in previous work, which was around the $2 \times 10^{-11}/\sqrt{\tau}$ level [17]. In these experiments, we utilised atom re-capture with a short experiment cycle time in order to minimise sequence dead time but retain the majority of the cold atoms. The higher short-term instability observed in this work is due to operation with a long experiment cycle time and no atom-recapture between experiment cycles. The longer cycle time is as a result of the installation of the mechanical shutter in the trapping beam to enable better extinction of the light used for laser-cooling. The shutter was implemented to mitigate against light shifts resulting from light leakage in the AOM used to switch the cooling light. However, the physical movement of the shutter limited how quickly the experiment cycle could be repeated and hence a full MOT load was used. Previous data also showed a strong plateau in the stability around 1×10^{-11}, [17], which does not appear in the data shown in Fig. 6. We attribute this to the implementation of magnetic shielding and improvements in the laboratory environmental control. The magnetic shielding reduced sensitivity to ambient magnetic fields , with an improvement of a factor of 2 at $\tau = 100\,\text{s}$. Re-implementation of atom-recapture between cycles [18] will be an interesting avenue in the future for improvements in the short-term stability.

At this stage, the limits to the measured stability are attributed to noise limits in our detection system as well as a residual sensitivity to drifting polarisation of the CPT field components from temperature-sensitivity of the polarization-extinction ratio of optical fibres. The latter will be improved upon with better cladding and environmental control of the optical bench.

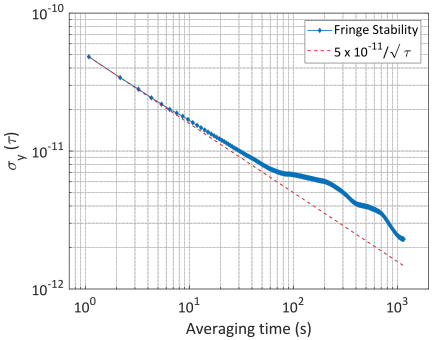

Fig. 6: The measured stability of the central Ramsey fringe in free-running mode shown by the blue data points. The red dashed line represents the short-term stability at $5 \times 10^{-11}/\sqrt{\tau}$.

6 Conclusion

We present recent progress with our compact, laser-cooled ^{87}Rb CPT atomic clock based on a grating magneto-optical trap. Here, we have implemented magnetic shielding around the GMOT ensemble and a mechanical shutter to eliminate leakage of the cooling light during the clock interrogation. With the lin⊥lin polarisation scheme and a Raman-Ramsey sequence, we have measured a short-term stability of $5 \times 10^{-11}/\sqrt{\tau}$ and encouraging evidence of stability in the mid-10^{-12} range. An investigation that combines this promising behaviour with a faster cycle time is an important future goal. In addition, a comprehensive study of systematic shifts of the clock frequency that result from using CPT interrogation, such as Doppler and AC-Stark shifts, should also be undertaken. Our long-term aim is the development of this system towards a completely compact cold-atom microwave clock.

Acknowledgment: We gratefully thank Dr Greg Hoth for his excellent work and support in driving the project.

Funding: The authors acknowledge financial support from EPSRC through the UK Quantum Technology Hub for Sensors and Metrology/Timing (EP/M013294/1, EP/T001046/1) and from the Defence Science and Technology Laboratory (DSTLX1000138605).

The data supporting this publication can be accessed at: https://doi.org/10.15129/4e8355df-93df-4157-a0cb-44953ff3dd20

References

[1] A. D. Ludlow, M. M. Boyd, J. Ye, E. Peik, and P. Schmidt, Rev. Mod. Phys. **87**, 637 (2015).

[2] N. Huntemann, C. Sanner, B. Lipphardt, C. Tamm, and E. Peik, Phys. Rev. Lett. **116**, 063001 (2016).

[3] S. L. Campbell, R. B. Hutson, G. E. Marti, A. Goban, N. Darkwah Oppong, R. L. McNally, L. Sonderhouse, J. M. Robinson, W. Zhang, B. J. Bloom, and J. Ye, Science **358**, 90 (2017).

[4] S. M. Brewer, J.-S. Chen, A. M. Hankin, E. R. Clements, C. W. Chou, D. J. Wineland, D. B. Hume, and D. R. Leibrandt, Phys. Rev. Lett. **123**, 033201 (2019).

[5] S. B. Koller, J. Grotti, S. Vogt, A. Al-Masoudi, S. Dörscher, S. Häfner, U. Sterr, and C. Lisdat, Phys. Rev. Lett. **118**, 073601 (2017).

[6] J. Grotti, S. Koller, S. Vogt, S. Häfner, U. Sterr, C. Lisdat, H. Denker, C. Voigt, L. Timmen, A. Rolland, F. N. Baynes, H. S. Margolis, M. Zampaolo, P. Thoumany, M. Pizzocaro, B. Rauf, F. Bregolin, A. Tampellini, P. Barbieri, M. Zucco, G. A. Costanzo, C. Clivati, F. Levi, and D. Calonico, Nature Physics **14**, 437 (2018).

[7] "MuQuans MuClock," https://www.muquans.com/product/muclock, [Accessed: 2020-05-27].

[8] "Spectradynamics cRb-Clock," https://spectradynamics.com/products/crb-clock/, [Accessed: 2020-05-27].

[9] B. Pelle, B. Desruelle, R. Szmuk, and D. Holleville, in *2017 Joint Conference of the European Frequency and Time Forum and IEEE International Frequency Control Symposium (EFTF/IFCS)* (2017).

[10] R. J. Hendricks, F. Ozimek, K. Szymaniec, B. Nagórny, P. Dunst, J. Nawrocki, S. Beattie, B. Jian, and K. Gibble, in *IEEE Transactions on Ultrasonics, Ferroelectrics, and Frequency Control* (2018) pp. 1–1.

[11] F. G. Ascarrunz, Y. O. Dudin, M. C. Delgado Aramburo, L. I. Ascarrunz, J. Savory, A. Banducci, and S. R. Jefferts, in *2018 IEEE International Frequency Control Symposium (IFCS)* (2018).

[12] C. C. Nshii, M. Vangeleyn, J. P. Cotter, P. F. Griffin, E. A. Hinds, C. N. Ironside, P. See, A. G. Sinclair, E. Riis, and A. S. Arnold, Nature Nanotech. **8**, 321 (2013).

[13] J. P. McGilligan, P. F. Griffin, R. Elvin, S. J. Ingleby, E. Riis, and A. S. Arnold, Sci. Rep. **7**, 384 (2017).

[14] G. W. Hoth, B. Pelle, S. Riedl, J. Kitching, and E. A. Donley, Appl. Phys. Lett. **109**, 071113 (2016).

[15] X.-H. Bao, A. Reingruber, P. Dietrich, J. Rui, A. Dück, T. Strassel, L. Li, N.-L. Liu, B. Zhao, and J.-W. Pan, Nature Phys. **8**, 517 (2012).

[16] "Kelvin Nanotechnology gMOT," https://www.kntnano.com, [Accessed: 2020-05-27].

[17] R. Elvin, G. W. Hoth, M. Wright, B. Lewis, J. P. McGilligan, A. S. Arnold, P. F. Griffin, and E. Riis, Opt. Express **27**, 38359 (2019).

[18] G. W. Hoth, R. Elvin, M. Wright, B. Lewis, A. S. Arnold, P. F. Griffin, and E. Riis, in *Proc. SPIE 10934, Optical, Opto-Atomic, and Entanglement-Enhanced Precision Metrology* (2019).

[19] J. Vanier, Appl. Phys. B **81**, 421 (2005).

[20] S. Knappe, V. Shah, P. D. D. Schwindt, L. Hollberg, J. Kitching, L.-A. Liew, and J. Moreland, Appl. Phys. Lett. **85**, 1460 (2004).

[21] A. V. Taichenachev, V. I. Yudin, V. L. Velichansky, and S. A. Zibrov, JETP Lett. **82**, 398 (2005).

[22] E. Blanshan, S. M. Rochester, E. A. Donley, and J. Kitching, Phys. Rev. A **91**, 041401 (2015).

[23] F.-X. Esnault, E. Blanshan, E. N. Ivanov, R. E. Scholten, J. Kitching, and E. A. Donley, Phys. Rev. A **88**, 042120 (2013).

[24] T. Zanon, S. Guerandel, E. de Clercq, D. Holleville, N. Dimarcq, and A. Clairon, Phys. Rev. Lett. **94**, 193002 (2005).

[25] C. Xi, Y. Guo-Qing, W. Jin, and Z. Ming-Sheng, Chin. Phys. Lett. **27**, 113201 (2010).

[26] M. Abdel Hafiz, G. Coget, P. Yun, S. Guérandel, E. de Clercq, and R. Boudot, J. Appl. Phys. **121**, 104903 (2017).

[27] S. V. Kargapoltsev, J. Kitching, L. Hollberg, A. V. Taichenachev, V. L. Velichansky, and V. I. Yudin, Laser Physics Letters **1**, 495 (2004).
[28] X. Liu, V. I. Yudin, A. V. Taichenachev, J. Kitching, and E. A. Donley, Appl. Phys. Lett. **111**, 224 (2017).
[29] J. D. Elgin, T. P. Heavner, J. Kitching, E. A. Donley, J. Denney, and E. A. Salim, Appl. Phys. Lett. **115**, 033503 (2019).
[30] G. W. Hoth, R. Elvin, M. W. Wright, B. Lewis, A. S. Arnold, P. F. Griffin, and E. Riis, in *2019 Joint Conference of the European Frequency and Time Forum and IEEE International Frequency Control Symposium (EFTF/IFCS)* (2019).
[31] X. Liu, E. Ivanov, V. I. Yudin, J. Kitching, and E. A. Donley, Phys. Rev. Appl. **8**, 054001 (2017).
[32] Z. Warren, M. S. Shahriar, R. Tripathi, and G. S. Pati, Metrologia **54**, 418 (2017).
[33] R. Elvin, G. W. Hoth, M. W. Wright, J. P. McGilligan, A. S. Arnold, P. F. Griffin, and E. Riis, in *2018 European Frequency and Time Forum (EFTF)* (2018) pp. 61–64.
[34] R. Boudot, S. Guerandel, E. d. Clercq, N. Dimarcq, and A. Clairon, in *2009 IEEE Transactions on Instrumentation and Measurement*, Vol. 58 (2009) pp. 1217–1222.
[35] M. Shuker, J. W. Pollock, V. I. Yudin, J. Kitching, and E. A. Donley, arXiv:1909.02649 [physics.atom-ph] (2019).